Soft X-ray spectroscopy of nanoparticles by velocity map imaging

O. Kostko, B. Xu, M. I. Jacobs, and M. Ahmed

Citation: The Journal of Chemical Physics **147**, 013931 (2017); doi: 10.1063/1.4982822
View online: http://dx.doi.org/10.1063/1.4982822
View Table of Contents: http://aip.scitation.org/toc/jcp/147/1
Published by the American Institute of Physics

Soft X-ray spectroscopy of nanoparticles by velocity map imaging

O. Kostko,[1] B. Xu,[1] M. I. Jacobs,[1,2] and M. Ahmed[1]
[1]*Chemical Sciences Division, Lawrence Berkeley National Laboratory, Berkeley, California 94720, USA*
[2]*Department of Chemistry, University of California, Berkeley, California 94720, USA*

(Received 8 February 2017; accepted 19 April 2017; published online 5 May 2017)

Velocity map imaging (VMI), a technique traditionally used to study chemical dynamics in the gas phase, is applied here to study X-ray photoemission from aerosol nanoparticles. Soft X-rays from the Advanced Light Source synchrotron, probe a beam of nanoparticles, and the resulting photoelectrons are velocity mapped to obtain their kinetic energy distributions. A new design of the VMI spectrometer is described. The spectrometer is benchmarked by measuring vacuum ultraviolet photoemission from gas phase xenon and squalene nanoparticles followed by measurements using soft X-rays. It is demonstrated that the photoelectron distribution from X-ray irradiated squalene nanoparticles is dominated by secondary electrons. By scanning the photon energies and measuring the intensities of these secondary electrons, a near edge X-ray absorption fine structure (NEXAFS) spectrum is obtained. The NEXAFS technique is used to obtain spectra of aqueous nanoparticles at the oxygen K edge. By varying the position of the aqueous nanoparticle beam relative to the incident X-ray beam, evidence is presented such that the VMI technique allows for NEXAFS spectroscopy of water in different physical states. Finally, we discuss the possibility of applying VMI methods to probe liquids and solids via X-ray spectroscopy. [http://dx.doi.org/10.1063/1.4982822]

INTRODUCTION

Photoemission is an extremely powerful method that probes the electronic structure of complex molecules. From its initial use in probing the electronic structure of freshly cleaved single crystals in an ultra-high vacuum environment[1] to its current application in systems relevant to electrochemistry, catalysis, and interfacial science,[2–5] the photoemission field has matured considerably over the last half century. When coupled with tunable photon sources, the technique allows for the probing of systems that have not been traditionally accessible.

Probing chemistry in aqueous systems with photoemission is a current topic of interest. However, the high vapor pressure of liquid water makes operating in a traditional high vacuum environment nearly impossible and also leads to scattering losses of the emitted electrons. A popular approach to overcome this problem is to reduce the surface area of the liquid, which minimizes evaporation of water molecules. Current implementations of this approach include: liquid microjet,[6–8] microdroplets,[9] and aerosols.[10–12] Another successful approach to deal with the high vapor pressure of the solvent is to improve the differential pumping scheme of the electron analyzer and move it closer to the probing region. This was started by Siegbahn and Siegbahn[13] in the 1970s and first implemented at a synchrotron light source by Bluhm, Salmeron, and co-workers.[14,15]

The pioneering work of Faubel *et al.* implemented vacuum ultraviolet (VUV) photoelectron spectroscopy on liquid microjets.[6] This led to studies on the electronic structure of liquids and solvated molecules, including pure water[6,7] and solvated biomolecules.[8] Recently, liquid microjets have been used in novel regimes, such as probing the solid-liquid interface using nanoparticles dissolved in a solvent.[16–19] Both X-ray photoelectron spectroscopy (XPS)—using hemispherical energy analyzers—and near edge X-ray absorption fine structure (NEXAFS) spectroscopy[20,21] have been applied to liquid microjets. The microdroplet probing technique is a modification of the liquid microjet experiment. The liquid jet can be split into a highly uniform droplet train which can be probed via ambient pressure XPS[9] or NEXAFS spectroscopy techniques. Although the approach has some advantages over the liquid jet technique, it has not received wide application.

Ahmed, Wilson, and co-workers pioneered the implementation of photoelectron spectroscopy of unsupported, gas-phase aerosols by using an aerodynamic lens for particle focusing coupled to a velocity map imaging (VMI) spectrometer. These first experiments, performed over a decade ago, were conducted on both inorganic[11,12,22] and organic[10] aerosols using tunable synchrotron VUV radiation. The technique of photoelectron spectroscopy of aerosol nanoparticles has been subsequently applied to the investigation of various systems. For example, an aerodynamic lens coupled to a hemispherical analyzer was used to perform valence band photoelectron spectroscopy of aqueous aerosols of biomolecules, which observed changes in the charge-transfer mechanism at different pH conditions of a solvent.[23,24] A similar setup has been used at synchrotron SOLEIL to investigate solid silicon[25] and flame generated (soot) nanoparticles[26] by means of XPS and NEXAFS. The spectroscopies performed at the carbon 1*s* edge compared the oxidation states of the surface (detected by XPS) and bulk (shown by NEXAFS) of soot nanoparticles.[26] The group of Signorell has begun a series of studies using a tunable synchrotron and lab based VUV radiation to extract a low energy electron mean free path in nanoparticles

using a VMI spectrometer coupled to an aerodynamic lens system.[27,28] A VMI spectrometer coupled to an aerodynamic lens and an ultrafast laser was used to understand the interaction of intense laser fields with isolated nanoparticles. The interaction of attosecond laser pulses with SiO_2 nanoparticles inside a VMI spectrometer visualized the collective electron motion in unsupported nanoparticles.[29] Another technique, termed "plasma explosion imaging," was used to study the absorption of strong femtosecond laser fields by isolated nanoparticles. In this case, ions generated after a nanoparticle absorbs a strong femtosecond pulse were velocity map imaged.[30]

VMI photoelectron spectroscopy of aerosols has numerous advantages over conventional photoelectron spectroscopy. For example, the absorption of a single photon per nanoparticle leads to the probing of a fresh nanoparticle surface. Single photon absorption limits the charging problem which is common in surface XPS. An added advantage of VMI spectroscopy is the collection of the 4π distribution of the emitted electrons, compared to the limited solid angle electron acceptance in hemispherical electron analyzers. Nevertheless, VMI spectrometers are constrained by their ability to accept electrons with the kinetic energy from zero to a finite maximum, which limits access to high kinetic energy electrons as well as limits energy resolution.

In this paper, we present the implementation of X-ray photoelectron and NEXAFS spectroscopies of unsupported gas-phase nanoparticles by velocity map imaging technique. We present a new VMI spectrometer design and collect known gas-phase and nanoparticle spectra to benchmark its performance. We present the preliminary NEXAFS spectra of aqueous nanoparticles and provide a tentative explanation of the observed results. We also discuss several possible applications of the VMI technique to study organic nanoparticles, biomolecules in aqueous environment, and possibilities for the investigation of aqueous systems.

EXPERIMENTAL METHODS

The photoelectron spectrometer was designed to detect electrons with the kinetic energy up to 100 eV and also to accommodate different types of samples: gas-phase molecules and unsupported nanoparticles. The final implementation of the experimental apparatus is shown in Fig. 1(a). The apparatus consists of an aerodynamic lens with two differential pumping regions (Fig. 1(a), left) and a VMI photoelectron spectrometer (Fig. 1(a), right).

The size of the imaging detector (Photonis PS32405, diameter of the active zone is 75 mm) and the highest practical voltage (8 kV) preset most aspects of the spectrometer design. To be able to detect electrons with the kinetic energy of 100 eV, the VMI electron optics need to be relatively compact. A four-electrode scheme was chosen to provide additional flexibility (Fig. 1(b)). The electrode El4 serves as a repeller, El3—extractor, El2—lens, and electrode El1 has a ground potential, which is the same as the front of the detector. Compared to the classic three electrode scheme,[31] the additional electrode El2 provides the possibility to improve the resolution of the spectrometer.

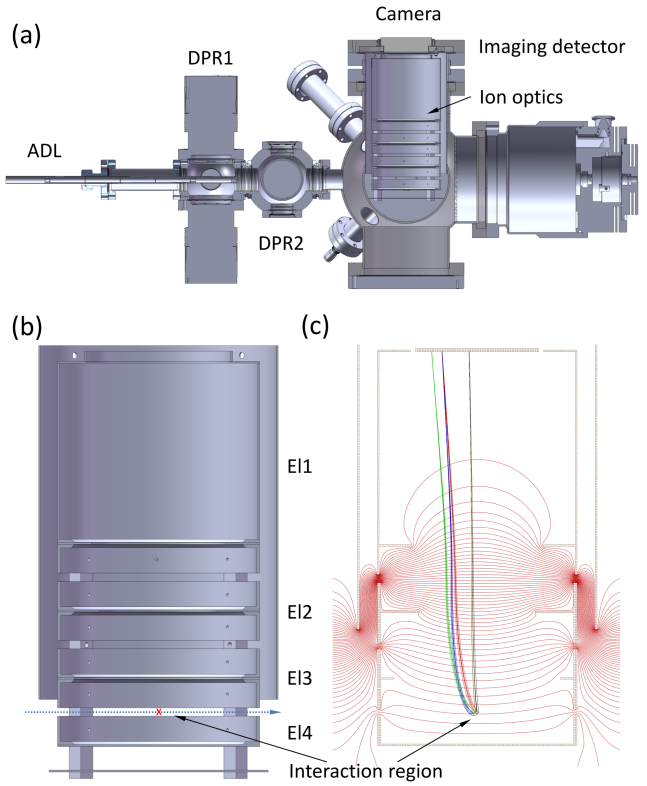

FIG. 1. Scheme of the velocity-map imaging photoelectron spectrometer. (a) Cross section of the apparatus. ADL—aerodynamic lens; DPR1, DPR2—differential pumping region 1 and 2. (b) Cross section of the VMI optics. El1–El4 stand for electrodes 1–4. The blue dotted line depicts the path of the nanoparticles. The red cross corresponds to the VUV/X-ray beam, propagating perpendicular to the plane of figure. (c) Simulation of ion optics (El1 = 0 V, El2 = −5500 V, El3 = −7360 V, El4 = −8000 V). Red lines depict equipotential contours (going from −157 V on top to −7843 V in bottom). Colored lines, going from an interaction region towards the detector on top, depict trajectories of electrons with a kinetic energy of 60 eV emitted at angles of 10°, 50°, 90°, 130°, and 170° with respect to the vertical axis of the VMI electron optics.

Simion 8.0 was used to design the final dimensions and positions of the VMI electrodes. The scripting functionality of Simion was utilized to automate the simulations. This consisted of changing the dimensions and positions of electrodes, generating a new ion optics geometry file, applying different voltages to the electrodes, and detecting positions of the electrons at the detector. The electrons were emitted at different angles to the vertical axis of the VMI optics and from slightly different initial positions (Fig. 1(c)). The spread between the positions of electrons which should hit the detector at the same location was used to determine the resolution of the spectrometer using the following relation:

$$\frac{\Delta KE}{KE} \cong \frac{2\Delta R}{R}, \tag{1}$$

where KE is the initial electron kinetic energy, R is the distance from the center of the detector to where the electron collision takes place, ΔKE and ΔR are the corresponding spreads (FWHM) in kinetic energy and distance. The best resolution of the spectrometer ($\Delta KE/KE$) of 1.0% was obtained in the simulations with the following geometries: a 220 mm length between the interaction region and the detector and 80 mm, 70 mm, and 100 mm openings in electrodes El1, El2, and El3,

respectively. To obtain a better picture of the spectrometer resolution, a more complex 3D model of the spectrometer was constructed in the Simion software and 100 000 electrons with the kinetic energy ranging from 10 to 100 eV in 10 eV increments were emitted from the interaction region. The electrons had a Gaussian spread in both their initial positions around the interaction region and their initial kinetic energies, and a random distribution of the initial directions. The simulation resulted in an image similar to the one obtained by the spectrometer's camera. This image was reconstructed using the same technique that is applied to the experimental data. The resolution of the spectrometer obtained from the 3D simulation was energy dependent (resolution was better for higher KE) and was 1.2% for 80 eV KE.

The final design based on the simulation is shown in Fig. 1(b). Each electrode has a side protection to avoid the perturbation of the electric field inside the spectrometer by external electric fields, such as those generated by wires, supplying the voltages to the electrodes. The electrodes are mounted on four plastic insulators that support the construction. The VMI optics are protected from magnetic fields by a cylindrical mu-metal shield, placed outside of the plastic electrode holders. Electrode El4 has a large opening covered by a metal mesh which reduces the number of background electrons generated by scattered light. The plate below El4 (Fig. 1(b)) can be used to attach either a nozzle to supply gas-phase samples or an oven to vaporize and introduce solid samples.

Electrons that reach the detector are first amplified by dual micro-channel plates and then hit a fast phosphor (P47) screen. The light generated by the electrons hitting the phosphor screen is detected using a camera with a CMOS sensor (Teledyne Dalsa Genie model TS-2048) coupled to a 25 mm fixed focal length lens. The parameters of the camera closely match those of the detector. The center-to-center spacing between the channels in the detector is 32 μm. Based on the 75 mm diameter of the detector's active zone, there are approximately 2344 channels across the detector, which closely resembles the camera resolution, 2048 × 2048 pixels. Images acquired by the camera are transferred to a PC via a network cable and accumulated by a LabVIEW program. The data are collected as two images: a signal image with sample present in the interaction region and a background image without the sample present in the interaction region. The difference between the two represents the image of electrons emitted by the sample. The pBASEX[32] algorithm was applied to reconstruct the velocity mapped images and extract photoemission spectra. Energy calibration of reconstructed spectra was performed by measuring the photoemission spectra of xenon at different photon energies. Nitrogen gas was used in place of xenon for photon energies greater than 100 eV.

Two different approaches were used to collect a NEXAFS spectrum using a VMI spectrometer. In the first approach, the NEXAFS spectra were collected by a camera, in the same way as photoelectron spectra. Because of the high secondary electron signal intensity, the NEXAFS images can be collected in less time than the photoelectron spectra with an acceptable signal to noise ratio. The intensity of the NEXAFS signal was extracted by integrating the electron signal in the central part of the velocity-map image (with kinetic energies below 10 eV). Another much faster technique used a photomultiplier tube to detect light from the phosphor screen instead of a camera. The tube collected only signal from the central part of the image, dominated by low energy secondary electrons (with kinetic energy <10 eV). Because of the additional signal amplification in the photomultiplier tube, the duration of signal collection at a single photon energy could be as short as 1 s (compared to 5–10 s in case of camera accumulation). The intensities of the signal collected by the camera or the photomultiplier tube signal were normalized by the photon flux, which was measured with a calibrated photodiode.

A system for the delivery of gas-phase nanoparticles is attached to the VMI photoelectron spectrometer chamber and consists of an aerodynamic lens coupled to two differential pumping regions (DPR1 and DPR2 in Fig. 1(a)). The differential pumping regions are needed to reduce the pressure from 760 Torr (atmospheric pressure) before the inlet of the aerodynamic lens to 10^{-6} Torr inside the VMI chamber. The lens was designed using an aerodynamic lens calculator.[33,34] A gas flow limiting aperture of 100–200 μm diameter is used as an inlet of the aerodynamic lens. To minimize the background signal generated by residual gas-phase contaminants, a liquid nitrogen cooled trap was installed inside the VMI spectrometer chamber. The high vacuum conditions in the chamber (base pressure of 10^{-8} Torr) and utilization of the trap minimized the background signal.

Nanoparticles are either generated via homogeneous nucleation or atomizing solutions. For homogeneous nucleation, nanoparticles are generated by passing dry nitrogen over a heated reservoir (150 °C) containing the pure compound of interest (squalene in this case). The cooling obtained as the flow leaves the oven, causes nanoparticles to nucleate. The size distributions of the nanoparticles are measured using a scanning mobility particle sizer (TSI, Model 3080). The diameters of the squalene nanoparticle are log-normal in distribution with an average diameter of ~220 ± 40 nm. To generate aqueous nanoparticles of water, solutions are atomized using a high flux atomizer (TSI, Model 3076). The size distribution of aqueous nanoparticles is broad, with the average diameter of 100 nm.

RESULTS

The performance of the VMI apparatus was tested on xenon gas, squalene, and water nanoparticles using tunable synchrotron radiation generated by VUV and soft X-ray beamlines 6.0.2, 6.3.2, 9.0.2, and 11.0.2 of the Advanced Light Source, Lawrence Berkeley National Laboratory. The bandwidth of the beamlines (0.1 to 0.2 eV) typically exceeds the intrinsic resolution of the VMI spectrometer. The VMI image collected by the apparatus for a gaseous xenon sample utilizing 22 eV VUV photons is shown in Figure 2(a). The two rings in Fig. 2(a) correspond to the Xe $5p_{1/2}$ (inner ring, kinetic energy of 8.6 eV) and $5p_{3/2}$ (outer ring, kinetic energy of 9.9 eV) lines. The VMI image of xenon collected with the photon energy of 80 eV also demonstrates a double ring (feature 1 in Figure 2(b)), which in this case corresponds to the emission of $4d_{3/2}$ (inner ring) and $4d_{5/2}$ (outer ring) electrons with kinetic energies of 10.5 eV and 12.5 eV, respectively.

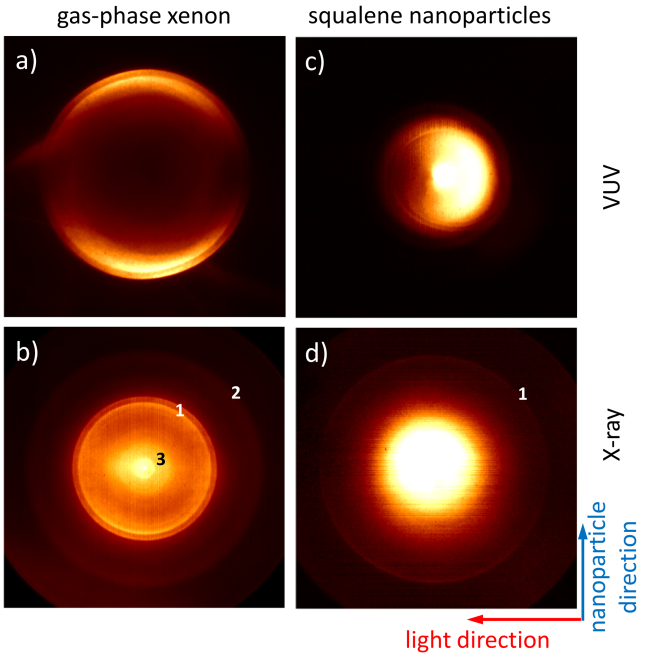

FIG. 2. Velocity map images of gas-phase and nanoparticle samples: (a) and (b) depict the spectra of gas-phase xenon measured at (a) 22 eV and (b) 80 eV photon energies. VMI spectra of squalene nanoparticles measured at (c) 15 eV and (d) 315 eV photon energies. The image feature labeled by 1 in panels (b) and (d) corresponds to photoelectrons. The dim ring labeled by 2 in panel (b) is due to the emission of Auger electrons. Feature 3 in panel (b) corresponds to double Auger decay. In panels (b) and (d) for large radii, the edge of the imaging detector is visible. The spectra in different panels are not shown to the same scale and are measured using different voltage settings.

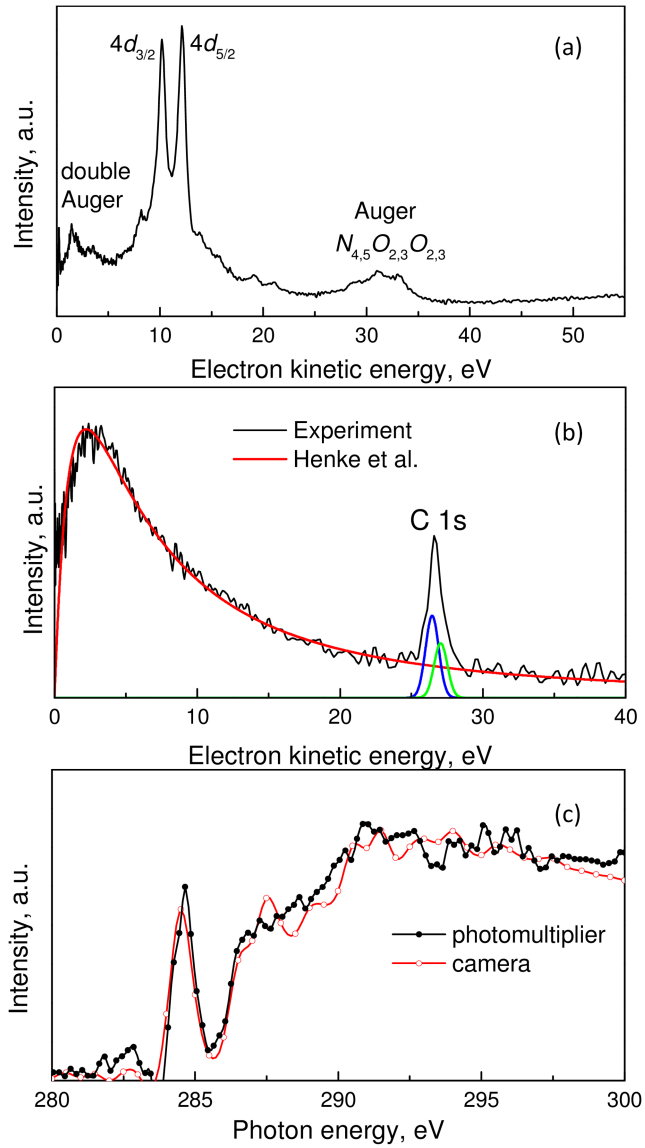

FIG. 3. (a) Reconstructed kinetic energy spectrum of xenon measured at photon energy of 80 eV. The spectrum corresponds to the image shown in Figure 2(b). (b) Reconstructed photoelectron spectrum of squalene, obtained using a photon energy of 315 eV. The corresponding image is shown in Figure 2(d). The experimental data (black line) is fitted using the secondary electron model of Henke *et al.*[42] (red line). C 1*s* photoelectrons are fitted by two Gaussian functions, corresponding to CHx (blue line) and C=C (green line) peaks. (c) NEXAFS spectrum of squalene nanoparticles measured with a photomultiplier tube (black line and filled circles) and with a camera (red line and open circles).

The photoelectron spectrum reconstructed from the image using the pBASEX algorithm is shown in Fig. 3(a). Another noticeable feature (labeled by 2 in Fig. 2(b)) is an additional ring of larger diameter and higher kinetic energy electrons, which has a lower intensity than that of the double ring. Its diameter is photon energy independent. The ring corresponds to the Auger $N_{4,5}O_{2,3}O_{2,3}$ decay of 4*d* holes, created during photoionization. The kinetic energy of Auger electrons within this feature lies in a range of 30–35 eV and correlates well with the literature data.[35,36] Two additional bright rings in the center of the image, labeled 3 in Fig. 2(b), are due to Xe 4*d* double Auger decay: sequential decay of holes generated in a primary Auger process. The double Auger process results in two rings, which correspond to electrons with a kinetic energy of 1.6 and 3.5 eV. Again, this correlates well with previous observations.[37,38]

VMI images of squalene nanoparticles measured using VUV (15 eV) and X-ray (315 eV) radiation are shown in Figures 2(c) and 2(d), respectively. The shallow penetration depth of VUV photons of less than 10 nm leads to preferential ionization and subsequent emission of electrons from the side of the nanoparticle directed toward the source of light. This image asymmetry observed in Figure 2(c) is caused by strong VUV light attenuation within the nanoparticle and was observed previously.[11,27,28] In contrast, X-ray photons have a light attenuation distance on the order of a few micrometers, which results in almost equal possibility of ionization of any molecule within a nanoparticle and leads to a symmetrical image (Fig. 2(d)). Feature 1 in Figure 2(d) corresponds to carbon 1*s* electrons emitted by squalene nanoparticles after the absorption of 315 eV photons. The kinetic energy of the emitted C 1*s* electrons is 26.7 eV in this case.

A large, bright, and symmetrical spot in the center of Fig. 2(d) appears due to the emission of secondary electrons, which are commonly observed in XPS measurements of bulk materials.[39] The absorption of an X-ray photon by a nanoparticle leads to the photoionization and emission of a C 1*s* electron (emission of a valence electron has lower probability due to significantly lower photoionization cross section). A C 1*s* hole predominantly decays via a *KLL* Auger process[40] leading to the emission of a second electron with a kinetic energy of

264 eV (not detected in this measurement).[41] Inelastic collisions of the energetic Auger electron (as well as of the photoelectron) with surrounding electrons lead to the emission of additional (secondary) electrons and to a reduction of the kinetic energy of the colliding primary (Auger or photo-) electrons. The corresponding reconstructed photoelectron spectrum generated from the image (Fig. 2(d)) is shown in Fig. 3(b). The spectrum has two pronounced features: a narrow, Gaussian-shaped peak at a kinetic energy of 26.7 eV and a fast-rising and exponentially decaying broad feature, peaking at 2.5–3.0 eV. The former peak corresponds to C 1*s* squalene photoelectrons, the latter is a broad secondary electron distribution.

A theoretical model developed by Henke *et al.* in the early era of X-ray photoelectron spectroscopy[42] was applied to fit the experimental distribution of secondary electrons observed in Fig. 3(b). The theoretical model assumes that the primary (photo- and Auger) electrons are responsible for the generation of secondary electrons and it takes into account both electron-electron and electron-phonon scattering during electron transport inside solids. The function proposed to fit the secondary electron emission spectrum from semiconductors and insulators is

$$I(E_K) = k\frac{E_K}{(E_K + E_A)^3}, \tag{2}$$

where I is the energy dependent signal intensity, k is a fitting coefficient, E_K is the electron kinetic energy, and E_A is the electron affinity energy. A similar formula was proposed by Henke *et al.* for modeling electron emission from metals, but with the denominator raised to the fourth power instead of the third power and the electron affinity replaced with a work function.[43] The fit of the experimental data shown in Fig. 3(b) results in an E_A of 4.4 eV. The electron affinity energy is included in the theoretical model as the energy reducing the kinetic energy of an electron, when it crosses a barrier between a solid and vacuum. The high value of the E_A suggests that in the case of a spherical nanoparticle, there is a significant barrier, reducing the kinetic energy of the escaping electrons. The E_A value obtained from the fit is on a par with values observed by Henke *et al.* for semiconductors and larger than those observed for insulators.[42] It should be noted that in their paper, the fit of the model to the experimental data was not very good for insulators.

From an analysis of the reconstructed photoelectron spectrum (Fig. 3(b)), it becomes obvious that the secondary electron signal dominates the spectrum and is many times stronger than the primary photoelectron peak. A similar behavior is observed in conventional X-ray photoelectron spectroscopy of bulk samples, where the majority of emitted electrons (from 50% to 90% according to Henke *et al.*[43]) have kinetic energies ranging from 0 to 30 eV.

Total electron yield is a common NEXAFS detection technique that measures the X-ray absorption of a material by detecting the emitted electrons with all kinetic energies.[44] These measured electrons are dominated by low kinetic energy secondary electrons that are similar to those observed here in the VMI spectra of nanoparticles. Therefore, by measuring the dependence of secondary electron intensity vs. excitation photon energy, a NEXAFS spectrum of unsupported nanoparticles can be obtained using a VMI spectrometer. An example of a carbon K edge NEXAFS spectrum of squalene nanoparticles collected using either a camera or a photomultiplier tube is shown in Figure 3(c). Both spectra demonstrate similar features, such as a separate peak at 284.6 eV from the carbon $1s \rightarrow \pi^*$ transition and a broad feature at higher photon energies from the transition of 1*s* electrons to the continuum of states. The small oscillations, observed in the spectra, arise from experimental noise.

DISCUSSION

XPS and NEXAFS techniques complement each other. XPS is a surface sensitive technique due to the short inelastic mean free path (IMFP) of electrons. The so-called "universal curve," which depicts the energy dependence of the electron IMFP, has a minimum around 30–100 eV kinetic energy, corresponding to an IMFP of 0.5–1 nm.[39,45] For lower kinetic energy electrons, the universal curve exhibits higher values of the IMFP, but there is an active discussion about the IMFP behavior at these energies.[7] Using photon energies that lead to the emission of electrons with kinetic energies ranging from 30 to 100 eV, XPS provides information on the electronic structure of the surface. Reducing the photon energy (which corresponds to a decrease in the kinetic energy of the emitted electron) leads to a larger probing depth. Thus, in contrast to XPS, the NEXAFS spectroscopy technique described above is more depth sensitive as it collects mostly low kinetic energy secondary electrons with longer IMFP.

Recently, the described techniques were applied to investigate kinetics of the ozonolysis of squalene nanoparticles.[46] The X-ray photoelectron spectroscopy was able to resolve peaks at the C 1*s* edge corresponding to differently bound carbon, such as C=C, CHx, C—O, and C=O bonds. The kinetics of the ozonolysis reaction were extracted from the analysis of the C=C peak decay with increased ozone exposure. A similar result was obtained from a NEXAFS measurement at the C and O K edges. In this particular case, XPS and NEXAFS measurements resulted in similar uptake coefficients despite the different probing depths of the methods. This was explained by the fact that squalene is a well-mixed liquid with a homogeneous composition.

Below we discuss the possibility of using X-ray photoelectron and NEXAFS spectroscopies on unsupported nanoparticles for the analysis of more complex systems such as liquids and solvated biomolecules. It is difficult to couple a liquid jet to a VMI spectrometer because of the close proximity of a high vapor pressure liquid to a pressure sensitive electron detector. However, nanoparticles generated from a solution of biomolecules passing through an aerodynamic lens have been studied via photoelectron spectroscopy, using either a VMI spectrometer[47] or a hemispherical analyzer,[23] providing information on the electronic structure of biomolecules in a liquid environment.

A NEXAFS spectrum at the oxygen K edge of aerosol nanoparticles generated from pure water is shown in Fig. 4(a).

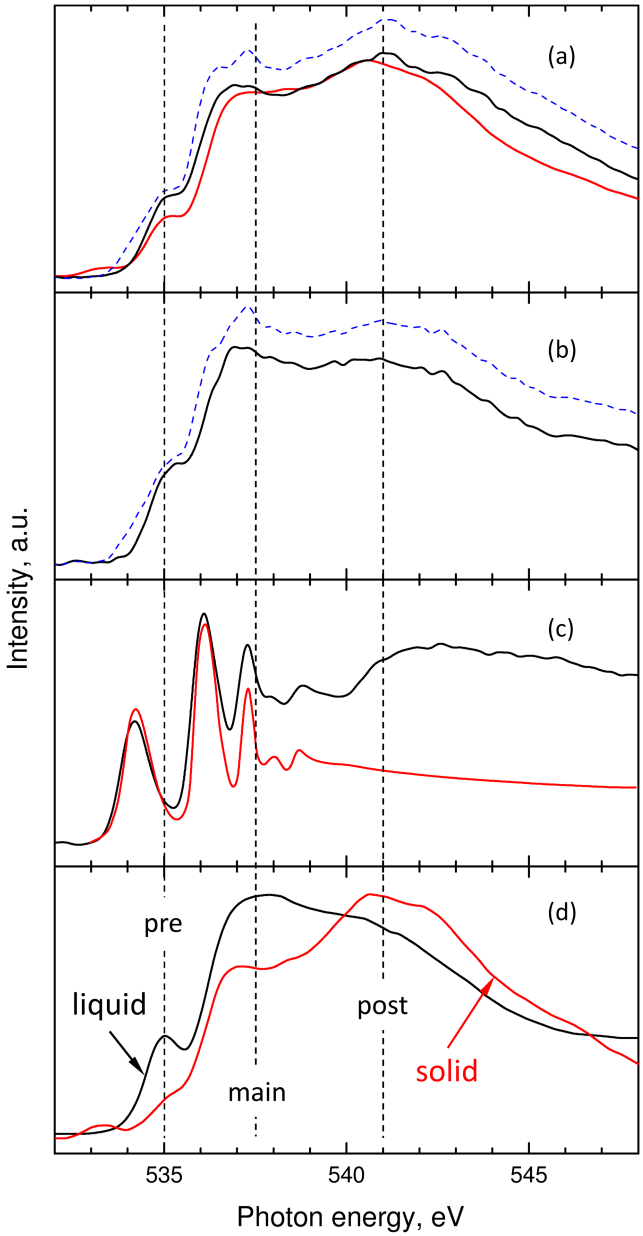

FIG. 4. NEXAFS oxygen K edge spectra (solid black lines) of (a) nanoparticles generated from pure water, (b) nanoparticles from a 0.038M solution of NaI in water, and (c) gas-phase water. Raw nanoparticle spectra (without subtracted gas-phase water component) are shown by the blue dashed lines in panels (a) and (b). For comparison, the literature[48] NEXAFS spectra are shown: red line in (a) composed of 40% liquid and 60% solid water NEXAFS, (c) gas-phase water NEXAFS spectrum is shown by red line, and (d) black line corresponds to liquid water NEXAFS and red line to solid water. Dashed vertical lines depict the positions of pre-, main-, and post-edges of water spectra observed in the NEXAFS data.[48]

A small addition of NaI to water (0.038M) changes the spectrum shape; the post-edge feature located around 541 eV becomes less intense (Fig. 4(b)). The NEXAFS spectrum of gas-phase water (Fig. 4(c)) is collected by moving the nanoparticle beam ~1 mm below the probing region. Although water nanoparticles are still present in the VMI spectrometer in this case, they do not interact with the X-ray beam, and the observed signal arises from the gas-phase water molecules that have evaporated from the nanoparticles. A good correlation of the current measurement to the previous data[48] is observed for gas-phase water in Fig. 4(c). Below we will provide a tentative explanation of the observed experimental results.

The pre-, main-, and post-edge features observed in the water NEXAFS spectra (Fig. 4(d), data from Ref. 48) are explained by different coordination of the H-bonding network. The pre-edge feature corresponds to weakened/nonexistent hydrogen bonding and to less coordinated water molecules. It is generally associated with the liquid state. The post-edge feature corresponds to the fully coordinated H-bonding network. For example, the enhancement of tetrahedral coordination in ice leads to an increase of the post-edge NEXAFS feature (and to a decrease of the pre-edge signal).[48] In the measured NEXAFS spectra, the post-edge feature intensity is stronger for nanoparticles generated from pure water than for nanoparticles from a 0.038M NaI solution. Such changes in the NEXAFS spectra have been observed from changes in the temperature (physical state)[49–51] of water and upon the introduction of solutes.[52,53]

As described above, a decrease in the water temperature leads to an increase of the post-edge peak and decrease of the pre-edge feature. This dependence has been experimentally observed previously for both liquid water and ice (see, e.g., References 49–51). The temperature of an aerosol in the VMI spectrometer is less defined than that in a liquid jet experiment. The aerosol nanoparticles are much smaller than the diameter of a liquid jet (hundreds of nanometers vs. ~10 μm) and, because of the differential pumping in the spectrometer, they travel a longer distance to the interaction region, which leads to extended evaporative cooling. According to estimates of Chang *et al.*, glutathione-water aerosol nanoparticles could exist in a deeply super cooled state, residing at ~193 K in the interaction region.[24] However, despite the very low temperature of the aerosol nanoparticles, the authors claim that spectral feature characteristics of liquid water are observed. Electron diffraction measurements conducted on the super cooled water nanodroplets revealed the existence of a liquid phase at temperatures as low as 200 K.[54] However, more recent coherent X-ray scattering measurements on micrometer sized water droplets have demonstrated a slightly larger liquid-ice transition point of 227 K, where only a tiny portion of droplets still remained liquid.[55]

The NEXAFS spectrum of pure water aerosol nanoparticles in Fig. 4(a) cannot be fit well by the literature data of either liquid water or ice, shown in Fig. 4(d).[48] The literature NEXAFS spectrum of liquid water has a stronger and better resolved pre-edge feature and less intense post-edge peak than that observed in Fig. 4(a), whereas the literature spectrum of ice has a smaller pre-edge and a stronger post-edge feature.[50] The NEXAFS spectrum of pure water aerosol could be fit by a linear combination of 40% liquid water and 60% ice NEXAFS spectra obtained from Ref. 48 (red line in Fig. 4(a)). This coexistence of liquid and ice nanoparticles could be a result of the broad size distribution (50–700 nm) of water nanoparticles used in the current experiment. This could lead to different cooling rates and temperatures of the nanoparticles in the probed region, resulting in the coexistence of the liquid and solid nanoparticles. A Raman thermometry setup, similar to that used in Ref. 56 (measuring

temperature of a liquid jet), is underway to quantify the aerosol temperature.

For the case of water nanoparticles, the ratio of surface to volume is about 450 times larger than that of a liquid microjet (assuming a 100 nm nanoparticle diameter and 30 μm microjet interacting with a 30 μm X-ray beam). This means that the signal component that originates from the surface should be stronger from nanoparticles than from a liquid jet. It was previously observed that the NEXAFS spectrum of the topmost layer of ice has a significantly different shape than the spectrum of bulk ice because the topmost layer has more water molecules with free O—H groups.[57] This results in an increase in the intensity of the pre-edge NEXAFS feature in spectra from the top layer of ice, which is redshifted by 0.4 eV in comparison to that of liquid water. This is not observed in Fig. 4(a), where the position of the pre-edge feature nicely correlates with that of liquid water (Fig. 4(d)).

The NEXAFS spectrum of a 0.038M aqueous solution of NaI (Fig. 4(b)) correlates well with pure water in the pre- and main-edges and has a substantially lower intensity of post-edge peak. Below we attempt to explain the observed deviation. Addition of salt to water depresses the freezing point of a solution. From Blagden's law (which states that a solution's freezing point depression is proportional to the concentration of the solute in the solution), the freezing point depression (ΔT) for the low NaI concentration used is $\Delta T = 0.14$ K. This negligible decrease of freezing temperature is not expected to affect the state of the aerosol significantly. However, preferential removal of water molecules during evaporative cooling may increase the NaI concentration in the nanoparticles. Chang *et al.* predicted the volume of nanoparticle decreases by 17% while they travel through vacuum to the interaction region.[24] The change in the volume leads to a ~20% increase in the NaI concentration.

Another effect of the NaI addition is the interaction of the resulting ions with the surrounding water molecules. It was previously observed that the shape of the oxygen K edge NEXAFS spectrum of water changes with the addition of salts. These spectral changes progressed as the salt concentration increased.[52,53] Similar changes were also observed in vibrational sum-frequency spectroscopy.[58] These changes are interpreted as iodide anions (which show a propensity for the interface)[59] weakening the water bonding coordination network near the surface region. The influence of the dissolved ions on the coordination of the water molecules in bulk water is still a subject of active discussion.[53,60–62] The observed reduction of the post-edge feature with the addition of NaI (Fig. 4(b)) could be rationalized as an increased concentration of iodide anions in the surface layer which leads to a perturbation of the tetrahedral coordination of water molecules. Although the previous studies employing a liquid microjet used much higher salt concentrations, the enhanced surface area to volume ratio in nanoparticles could magnify the observed post-edge signal increase. However, molecular dynamics simulations are required to understand the spectra completely.

Finally, we note that the VMI technique could be extended to study stationary liquids and surfaces, with the intentions of probing chemical reactions, solvation, photochemistry, or electrochemistry. There have been several approaches to study solid samples within a VMI spectrometer. Ions generated by post-desorption ionization were imaged using a VMI spectrometer and their velocities and distributions were studied.[63,64] It was found that a VMI spectrometer can also be used to measure the kinetic energy distribution of electrons emitted from a small solid target (e.g., a metal tip) inside a VMI spectrometer after interaction of the target with femtosecond laser radiation.[65,66] With proper modification of a VMI spectrometer, it should be possible to collect electrons emitted from a conductive surface. For this, the sample could be placed onto the repeller electrode (El4 in Fig. 1) and electrons will be emitted from the sample. In this case, a 4π collection efficiency would not be achieved. Rather, a 2π solid angle would be directed toward the detector. Even with this collection inefficiency, the obtained signal should be strong because every photon directed to the sample will be absorbed and may result in a photoelectron. To illuminate the sample by X-ray radiation, the VMI spectrometer should be tilted such that the X-ray beam passes through a gap between the repeller and the extractor electrodes and hits the sample attached to the center of the repeller. Previously, a liquid meniscus from a small orifice (2–5 μm) in a thin SiN film has been formed and probed in an UHV environment. Ions from this liquid surface were directly probed using secondary ion mass spectrometry.[67] We are currently implementing this device within our VMI spectrometer in order to perform photoelectron spectroscopy of liquids. Because the majority of the X-ray beam will hit the sample holder and only a small portion of the beam will be absorbed by the liquid meniscus, strong backgrounds are expected to interfere with these measurements. Because of this, careful measurement and subtraction of the background signal from the sample holder without the probing liquid will be important.

CONCLUSIONS

This study describes a velocity map imaging photoelectron spectrometer and its application for X-ray photoemission experiments on unsupported nanoparticles. The photoelectron spectrometer capable of collecting electrons with kinetic energy up to 100 eV was commissioned using tunable synchrotron radiation and gas phase samples. The X-ray photoelectron spectra of organic nanoparticles measured at the carbon K-edge demonstrate a strong low kinetic energy background, which is explained as emission of secondary electrons caused by inelastic scattering of Auger electrons. It is demonstrated that the signal of the low kinetic energy secondary electrons can be used to perform NEXAFS spectroscopy of unsupported nanoparticles. Oxygen 1*s* NEXAFS spectra of water nanoparticles (prepared from pure water and 0.038M NaI solution) and of gas-phase water molecules are presented. The observed spectral features are explained in terms of coexisting frozen and liquid nanoparticles and a perturbation of tetrahedral molecular coordination by iodide anions in the surface layer of aqueous NaI nanoparticles. Finally, we provide a brief outlook on applications of VMI for investigation of liquids and solutions.

ACKNOWLEDGMENTS

This work and the Advanced Light Source are supported by the Director, Office of Science, Office of Basic Energy Sciences, of the U.S. Department of Energy under Contract No. DE-AC02-05CH11231, through the Chemical Sciences Division. M.I.J. thanks the NSF for an NSF Graduate Research Fellowship under No. DGE-1106400. O.K. is thankful to Kevin R. Wilson and Hendrik Bluhm for fruitful discussions. M.A. acknowledges support from LBNL—laboratory directed research and development for the water aspect of this work. The authors acknowledge help of Elio Champenois, who developed Matlab and Python implementations of pBASEX code used in the current paper.[68]

[1] *ESCA - Atomic, Molecular and Solid State Structure Studied by Means of Electron Spectroscopy*, edited by K. Siegbahn (Almqvist & Wiksells, Uppsala, 1967).
[2] R. Seidel, B. Winter, and S. E. Bradforth, Annu. Rev. Phys. Chem. **67**, 283 (2016).
[3] K. M. Lange and E. F. Aziz, Chem. Soc. Rev. **42**, 6840 (2013).
[4] L. Trotochaud, A. R. Head, O. Karslıoğlu, L. Kyhl, and H. Bluhm, J. Phys.: Condens. Matter **29**, 053002 (2017).
[5] E. J. Crumlin, Z. Liu, H. Bluhm, W. Yang, J. Guo, and Z. Hussain, J. Electron Spectrosc. Relat. Phenom. **200**, 264 (2015).
[6] M. Faubel, B. Steiner, and J. P. Toennies, J. Chem. Phys. **106**, 9013 (1997).
[7] S. Thürmer, R. Seidel, M. Faubel, W. Eberhardt, J. C. Hemminger, S. E. Bradforth, and B. Winter, Phys. Rev. Lett. **111**, 173005 (2013).
[8] N. Ottosson, K. J. Børve, D. Spångberg, H. Bergersen, L. J. Sæthre, M. Faubel, W. Pokapanich, G. Öhrwall, O. Björneholm, and B. Winter, J. Am. Chem. Soc. **133**, 3120 (2011).
[9] D. E. Starr, E. K. Wong, D. R. Worsnop, K. R. Wilson, and H. Bluhm, Phys. Chem. Chem. Phys. **10**, 3093 (2008).
[10] K. R. Wilson, D. S. Peterka, M. Jimenez-Cruz, S. R. Leone, and M. Ahmed, Phys. Chem. Chem. Phys. **8**, 1884 (2006).
[11] K. R. Wilson, S. Zou, J. Shu, E. Rühl, S. R. Leone, G. C. Schatz, and M. Ahmed, Nano Lett. **7**, 2014 (2007).
[12] J. Shu, K. R. Wilson, M. Ahmed, and S. R. Leone, Rev. Sci. Instrum. **77**, 043106 (2006).
[13] H. Siegbahn and K. Siegbahn, J. Electron Spectrosc. Relat. Phenom. **2**, 319 (1973).
[14] D. F. Ogletree, H. Bluhm, G. Lebedev, C. S. Fadley, Z. Hussain, and M. Salmeron, Rev. Sci. Instrum. **73**, 3872 (2002).
[15] D. E. Starr, Z. Liu, M. Hävecker, A. Knop-Gericke, and H. Bluhm, Chem. Soc. Rev. **42**, 5833 (2013).
[16] M. A. Brown, I. Jordan, A. Beloqui Redondo, A. Kleibert, H. J. Wörner, and J. A. van Bokhoven, Surf. Sci. **610**, 1 (2013).
[17] M. A. Brown, R. Seidel, S. Thürmer, M. Faubel, J. C. Hemminger, J. A. van Bokhoven, B. Winter, and M. Sterrer, Phys. Chem. Chem. Phys. **13**, 12720 (2011).
[18] J. Söderström, N. Ottosson, W. Pokapanich, G. Öhrwall, and O. Björneholm, J. Electron Spectrosc. Relat. Phenom. **184**, 375 (2011).
[19] M. J. Makowski, R. P. Galhenage, J. Langford, and J. C. Hemminger, J. Phys. Chem. Lett. **7**, 1732 (2016).
[20] B. M. Messer, C. D. Cappa, J. D. Smith, K. R. Wilson, M. K. Gilles, R. C. Cohen, and R. J. Saykally, J. Phys. Chem. B **109**, 5375 (2005).
[21] D. Nolting, E. F. Aziz, N. Ottosson, M. Faubel, I. V. Hertel, and B. Winter, J. Am. Chem. Soc. **129**, 14068 (2007).
[22] M. J. Berg, K. R. Wilson, C. M. Sorensen, A. Chakrabarti, and M. Ahmed, J. Quant. Spectrosc. Radiat. Transfer **113**, 259 (2012).
[23] C.-C. Su, Y. Yu, P.-C. Chang, Y.-W. Chen, I.-Y. Chen, Y.-Y. Lee, and C. C. Wang, J. Phys. Chem. Lett. **6**, 817 (2015).
[24] P.-C. Chang, Y. Yu, Z.-H. Wu, P.-C. Lin, W.-R. Chen, C.-C. Su, M.-S. Chen, Y.-L. Li, T.-P. Huang, Y.-Y. Lee, and C. C. Wang, J. Phys. Chem. B **120**, 10181 (2016).
[25] O. Sublemontier, C. Nicolas, D. Aureau, M. Patanen, H. Kintz, X. Liu, M.-A. Gaveau, J.-L. Le Garrec, E. Robert, F.-A. Barreda, A. Etcheberry, C. Reynaud, J. B. Mitchell, and C. Miron, J. Phys. Chem. Lett. **5**, 3399 (2014).
[26] F.-X. Ouf, P. Parent, C. Laffon, I. Marhaba, D. Ferry, B. Marcillaud, E. Antonsson, S. Benkoula, X.-J. Liu, C. Nicolas, E. Robert, M. Patanen, F.-A. Barreda, O. Sublemontier, A. Coppalle, J. Yon, F. Miserque, T. Mostefaoui, T. Z. Regier, J.-B. A. Mitchell, and C. Miron, Sci. Rep. **6**, 36495 (2016).
[27] M. Goldmann, J. Miguel-Sánchez, A. H. C. West, B. L. Yoder, and R. Signorell, J. Chem. Phys. **142**, 224304 (2015).
[28] R. Signorell, M. Goldmann, B. L. Yoder, A. Bodi, E. Chasovskikh, L. Lang, and D. Luckhaus, Chem. Phys. Lett. **658**, 1 (2016).
[29] S. Zherebtsov, T. Fennel, J. Plenge, E. Antonsson, I. Znakovskaya, A. Wirth, O. Herrwerth, F. Süßmann, C. Peltz, I. Ahmad, S. A. Trushin, V. Pervak, S. Karsch, M. J. J. Vrakking, B. Langer, C. Graf, M. I. Stockman, F. Krausz, E. Rühl, and M. F. Kling, Nat. Phys. **7**, 656 (2011).
[30] D. D. Hickstein, F. Dollar, J. L. Ellis, K. J. Schnitzenbaumer, K. E. Keister, G. M. Petrov, C. Ding, B. B. Palm, J. A. Gaffney, M. E. Foord, S. B. Libby, G. Dukovic, J. L. Jimenez, H. C. Kapteyn, M. M. Murnane, and W. Xiong, ACS Nano **8**, 8810 (2014).
[31] A. T. J. B. Eppink and D. H. Parker, Rev. Sci. Instrum. **68**, 3477 (1997).
[32] G. A. Garcia, L. Nahon, and I. Powis, Rev. Sci. Instrum. **75**, 4989 (2004).
[33] X. Wang and P. McMurry, Aerosol Sci. Technol. **40**, 320 (2006).
[34] X. Wang and P. H. McMurry, Aerosol Sci. Technol. **40**, 1 (2006).
[35] S. Ohtani, H. Nishimura, H. Suzuki, and K. Wakiya, Phys. Rev. Lett. **36**, 863 (1976).
[36] A. Kivimäki, L. Pfeiffer, H. Aksela, E. Nõmmiste, and S. Aksela, J. Electron Spectrosc. Relat. Phenom. **101–103**, 43 (1999).
[37] J. Viefhaus, M. Braune, S. Korica, A. Reinköster, D. Rolles, and U. Becker, J. Phys. B: At., Mol. Opt. Phys. **38**, 3885 (2005).
[38] F. Penent, J. Palaudoux, P. Lablanquie, L. Andric, R. Feifel, and J. H. D. Eland, Phys. Rev. Lett. **95**, 083002 (2005).
[39] S. Hüfner, in *Photoelectron Spectroscopy* (Springer, Berlin, Heidelberg, 1996), pp. 1–26.
[40] M. O. Krause, J. Phys. Chem. Ref. Data **8**, 307 (1979).
[41] J. F. Moulder, W. F. Stickle, P. E. Sobol, and K. D. Bomben, *Handbook of X-Ray Photoelectron Spectroscopy* (Physical Electronics, Inc., 1995).
[42] B. L. Henke, J. Liesegang, and S. D. Smith, Phys. Rev. B **19**, 3004 (1979).
[43] B. L. Henke, J. A. Smith, and D. T. Attwood, J. Appl. Phys. **48**, 1852 (1977).
[44] J. Stohr, *NEXAFS Spectroscopy* (Springer, Berlin, Heidelberg, 1996).
[45] M. P. Seah and W. A. Dench, Surf. Interface Anal. **1**, 2 (1979).
[46] M. I. Jacobs, B. Xu, O. Kostko, N. Heine, M. Ahmed, and K. R. Wilson, J. Phys. Chem. A **120**, 8645 (2016).
[47] B. Xu, M. I. Jacobs, O. Kostko, and M. Ahmed, "Guanidinium group is protonated in a strongly basic arginine solution," ChemPhysChem (in press).
[48] T. Fransson, Y. Harada, N. Kosugi, N. A. Besley, B. Winter, J. J. Rehr, L. G. M. Pettersson, and A. Nilsson, Chem. Rev. **116**, 7551 (2016).
[49] T. Pylkkänen, A. Sakko, M. Hakala, K. Hämäläinen, G. Monaco, and S. Huotari, J. Phys. Chem. B **115**, 14544 (2011).
[50] J. A. Sellberg, S. Kaya, V. H. Segtnan, C. Chen, T. Tyliszczak, H. Ogasawara, D. Nordlund, L. G. M. Pettersson, and A. Nilsson, J. Chem. Phys. **141**, 034507 (2014).
[51] H. Bluhm, D. F. Ogletree, C. S. Fadley, Z. Hussain, and M. Salmeron, J. Phys.: Condens. Matter **14**, L227 (2002).
[52] Y. L. Jeyachandran, F. Meyer, S. Nagarajan, A. Benkert, M. Bär, M. Blum, W. Yang, F. Reinert, C. Heske, L. Weinhardt, and M. Zharnikov, J. Phys. Chem. Lett. **5**, 4143 (2014).
[53] C. D. Cappa, J. D. Smith, K. R. Wilson, B. M. Messer, M. K. Gilles, R. C. Cohen, and R. J. Saykally, J. Phys. Chem. B **109**, 7046 (2005).
[54] L. S. Bartell and J. Huang, J. Phys. Chem. **98**, 7455 (1994).
[55] J. A. Sellberg, C. Huang, T. A. McQueen, N. D. Loh, H. Laksmono, D. Schlesinger, R. G. Sierra, D. Nordlund, C. Y. Hampton, D. Starodub, D. P. DePonte, M. Beye, C. Chen, A. V. Martin, A. Barty, K. T. Wikfeldt, T. M. Weiss, C. Caronna, J. Feldkamp, L. B. Skinner, M. M. Seibert, M. Messerschmidt, G. J. Williams, S. Boutet, L. G. M. Pettersson, M. J. Bogan, and A. Nilsson, Nature **510**, 381 (2014).
[56] J. D. Smith, C. D. Cappa, W. S. Drisdell, R. C. Cohen, and R. J. Saykally, J. Am. Chem. Soc. **128**, 12892 (2006).
[57] P. Wernet, D. Nordlund, U. Bergmann, M. Cavalleri, M. Odelius, H. Ogasawara, L. Å. Näslund, T. K. Hirsch, L. Ojamäe, P. Glatzel, L. G. M. Pettersson, and A. Nilsson, Science **304**, 995 (2004).
[58] E. A. Raymond and G. L. Richmond, J. Phys. Chem. B **108**, 5051 (2004).
[59] P. Jungwirth and D. J. Tobias, J. Phys. Chem. B **106**, 6361 (2002).
[60] N. Galamba, J. Phys. Chem. B **117**, 589 (2013).
[61] Y. Marcus, Chem. Rev. **109**, 1346 (2009).

[62]L.-Å. Näslund, D. C. Edwards, P. Wernet, U. Bergmann, H. Ogasawara, L. G. M. Pettersson, S. Myneni, and A. Nilsson, J. Phys. Chem. A **109**, 5995 (2005).
[63]S. P. K. Koehler, Y. Ji, D. J. Auerbach, and A. M. Wodtke, Phys. Chem. Chem. Phys. **11**, 7540 (2009).
[64]S. Abujarada, H. AlSalem, U. K. Chohan, G. L. Draper, and S. P. K. Koehler, J. Chem. Phys. **145**, 184201 (2016).
[65]A. R. Bainbridge and W. A. Bryan, New J. Phys. **16**, 103031 (2014).
[66]H. Ye, J. M. Kienitz, S. Fang, S. Trippel, M. Swanwick, P. D. Keathley, L. F. Velásquez-García, G. Cirmi, G. Rossi, A. Fallahi, O. D. Mücke, J. Küpper, and F. X. Kärtner, in *19th International Conference on Ultrafast Phenomena 2014 Paper 09WedP337* (Optical Society of America, 2014), p. 09, Wed.P3.37.
[67]L. Yang, X.-Y. Yu, Z. Zhu, T. Thevuthasan, and J. P. Cowin, J. Vac. Sci. Technol., A **29**, 061101 (2011).
[68]E. Champenois, CpBASEX, https://github.com/e-champenois/CPBASEX.